Supplementary Information (SI) for Soft Matter.
This journal is © The Royal Society of Chemistry 2025

Supporting Information

Genetic Control of Morphological Transitions in a Coacervating Protein Template

William C. Wixson[1], Nada Y. Naser[1], Aditya Sonpal[2], Jim Pfaendtner[2], François Baneyx[1*]

[1] Department of Chemical Engineering, University of Washington, Seattle, WA

[2] Department of Chemical & Biomolecular Engineering, North Carolina State University, Raleigh, NC

Corresponding Author

*François Baneyx – Department of Chemical Engineering, University of Washington, Seattle, Washington 98195, United States; orcid.org/0000-0001-5596-7903; Email: baneyx@uw.edu

Supplementary Methods

Molecular dynamics analysis

MD was performed using the leapfrog algorithm with a 2 fs time step facilitated by freezing all covalent bonds involving hydrogens using the LINCS algorithm.[1] Short-range electrostatic and van der Waals interactions were truncated at 1.1nm, while long range electrostatics were treated using the Particle Mesh Ewald (PME) method with grid spacing of 0.08 nm.[2] Temperature was maintained at 300 K using the stochastic velocity-rescaling thermostat,[3] and semi-isotropic pressure coupling (1 bar) was applied with the Berendsen barostat[4] (time constant: 1.0 ps; isothermal compressibility: 4.5×10^{-5} bar^{-1}), with pressure coupling uniformly restricted to the X and Y directions.

The simulation box was created with 9 ELP-linker-tag chains and 2500 water molecules using PACKMOL. These initial systems underwent energy minimization comprising 100,000 steepest descent steps followed by 100 ps of NVT equilibration, both with all the chains frozen in place to allow effective equilibration. The system was then solvated with SPC water molecules followed by minimization (100,000 steepest descent steps) and additional NVT (100 ps). Semi-isotropic pressure equilibration was conducted for 100 ns, followed by a 300 ns production run, both with unrestrained chains.[5]

We obtain the chain-chain and chain-water short-range Coulombic and Lennard Jones (LJ) energies for each of our ELP-linker-tag systems. We calculate the difference between these energies for each system from the ELP-Car9 system as a percentage of the ELP-Car9 energies as shown in the following equation.

$$E_{relative} = \frac{E_{ELP-Car9} - E_{ELP-tag}}{E_{ELP-Car9}} \times 100\% \ \#S1$$

We considered the trajectory from the last 100 ns of our production run from the three independent trials to calculate the end-to-end peptide distance (distance between the center of mass (COM) of the first and last residues of the peptide tag) for each peptide tag in our 9 ELP-linker-tag chains. We used this as a simple surrogate metric for compactness. We use the kernel density estimation (KDE) plots of the end-to-end peptide distances (**Fig. S11**) to show that based on the spread of peptide lengths across 9 chains and three independent trials, V5-Car9 and V5-P9AG10A remain more compact than the other variants in the polymer brush environment. The taller peak in the KDE of V5-Car9 also reveals that it remained more compact compared to V5-P9AG10A.

We combined the peptide trajectory segments from all 9 chains and three trials into one long 2.7 μs trajectory (9 chains × 1

$$H = -\sum_i p_i \log_2 p_i \quad \#S2$$

$$p_i = \frac{Size_{cluster}}{\sum Size_{cluster}} \#S3$$

Higher entropy is an indicator of greater conformational freedom and structural diversity. Taken together, the Shannon entropy (**Table S2**) values and the cumulative distribution function (CDF) of cluster sizes (**Figure S12**) show that V5-Car9 chains explored a broader range of conformations compared to V5-P9AG10A across all 9 chains and three independent trials. We tested this finding at additional cutoff values of 0.2 and 0.25 nm and found no significant differences.

Supplementary Figures

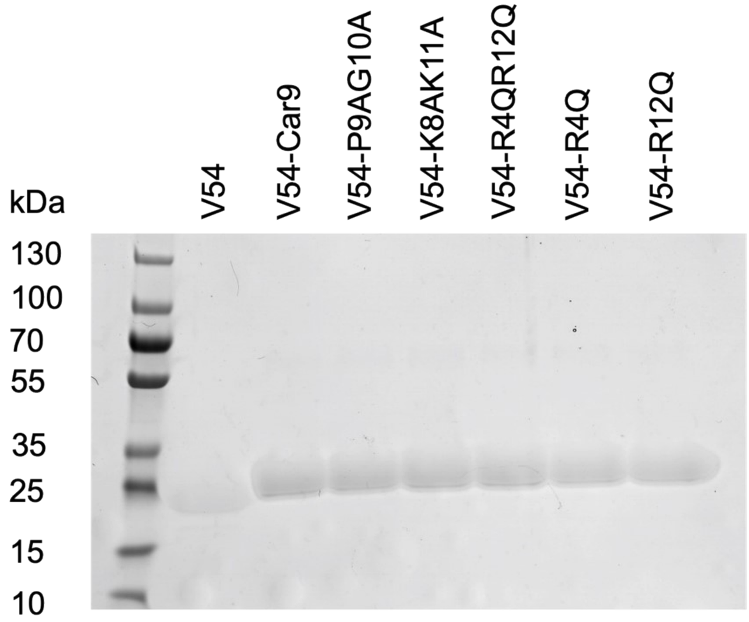

Figure S1. Coomassie blue-stained SDS-PAGE of the purified proteins used in this work.

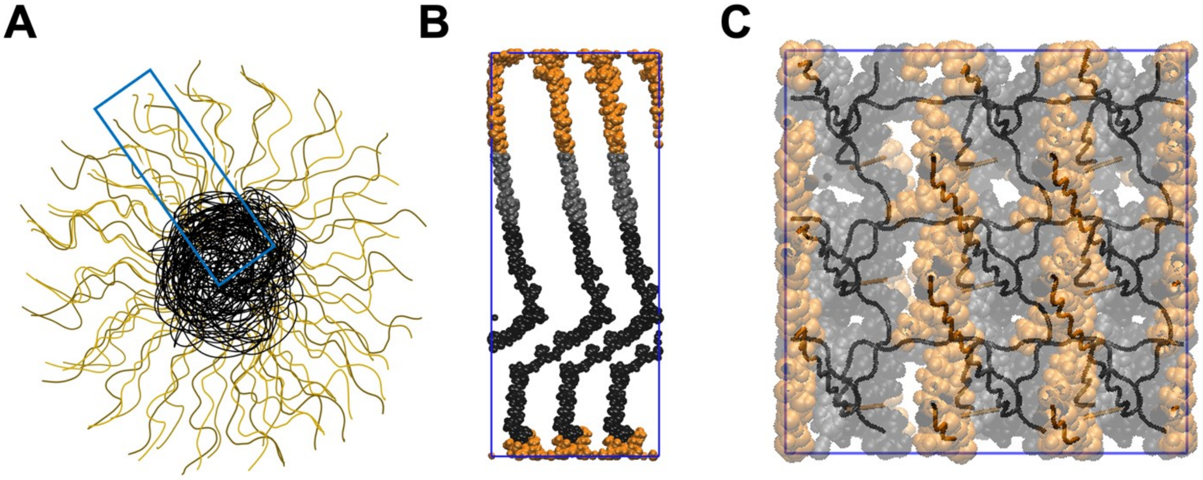

Figure S2. (A) The section of the micelle boxed in blue is represented as a polymer brush-like system in MD simulations. The starting configuration of the 3 x 3 grid of proteins with V5 segments in dark gray, linkers in light gray, and silica-binding segments in orange is shown in front (B) and top (C) views.

Table S1. Zeta potentials of mineralization products obtained with the indicated variants at 50°C

Variant	**ζ Potential (mV)**
V54-Car9	24 ± 3
V54-P9AG10A	26 ± 3
V54-K8AK11A	11 ± 2
V54-R4QR12Q	6 ± 1
V54-R4Q	6 ± 1
V54-R12Q	9 ± 1
V54-K7QK8QK11QR12Q	-1 ± 1

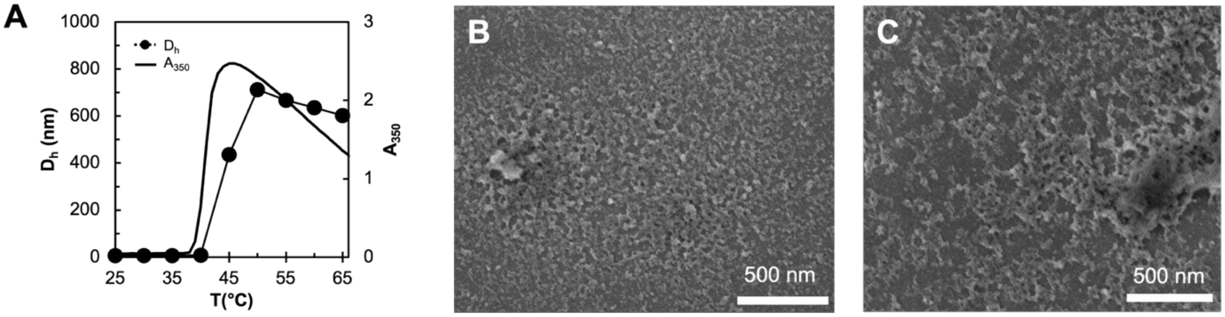

Figure S3. (A) Turbidity data (solid line) and hydrodynamic diameters (circles) were acquired in the 25°C to 65°C temperature range for the V54-K7QK8QK11QR12Q (V54-4Q) quadruple mutant which carries no net charge. (B-C) SEM images of mineralization products obtained at (B) 50 and (C) 65°C reveal no morphology control. Similar images were previously obtained with unfused V54.[8]

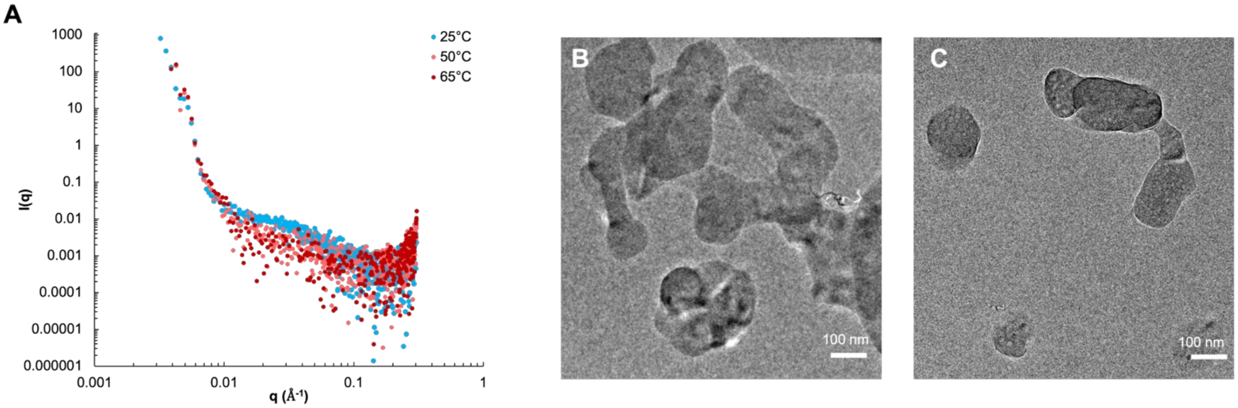

Figure S4. (A) SAXS data of V54-K8AK11A collected at 25, 50 and 65°C indicate a very weak scattering signal above the transition temperature. (B-C) Cryo-TEM images of V54-K8AK11A samples prepared at 65°C.

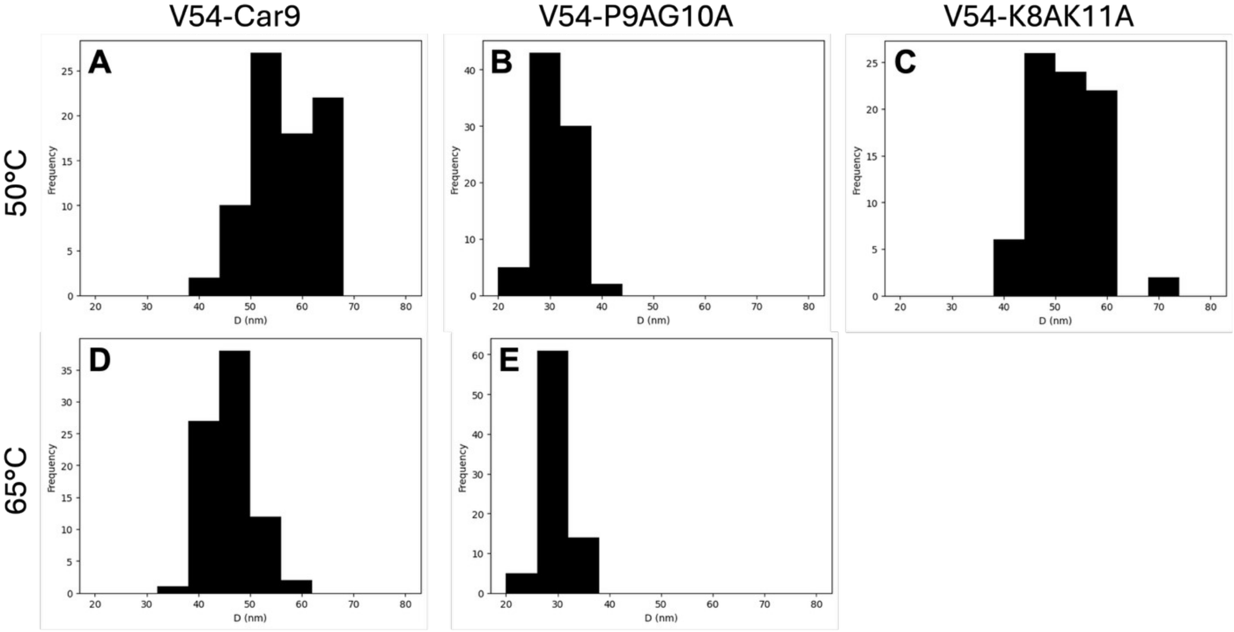

Figure S5. Histograms of particle diameters of micelle-templated silica particles mineralized in the presence of (A, D) V54-Car9 and (B,E) V54-P9AG10A at 50°C and 65°C, as well as (C) V54-K8AK11A at 50°C. Measured from SEM images, n=80.

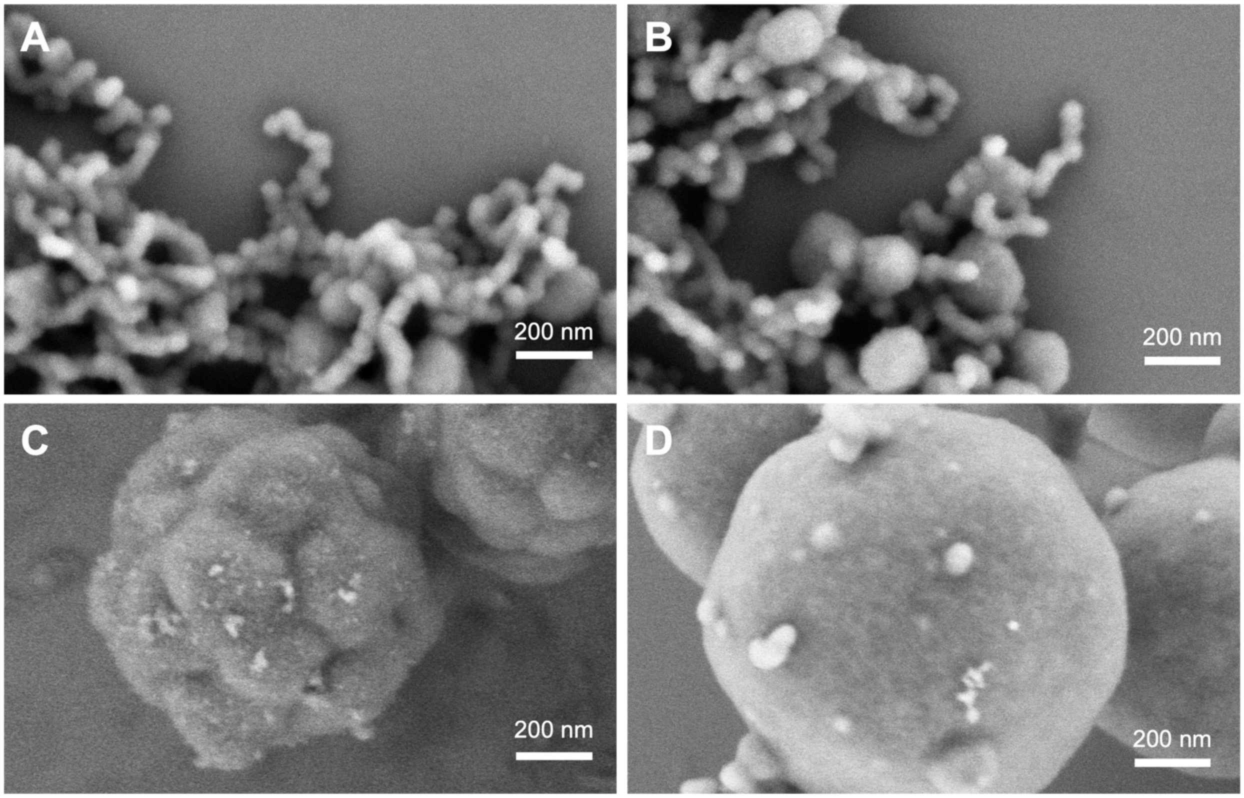

Figure S6. Representative SEM images of the various morphologies accessed by V54-R4QR12Q at 50ºC: (A) interconnected micelles; (B) primary vesicles; (C) raspberry vesicles; and (D) large vesicles/proteinosomes.

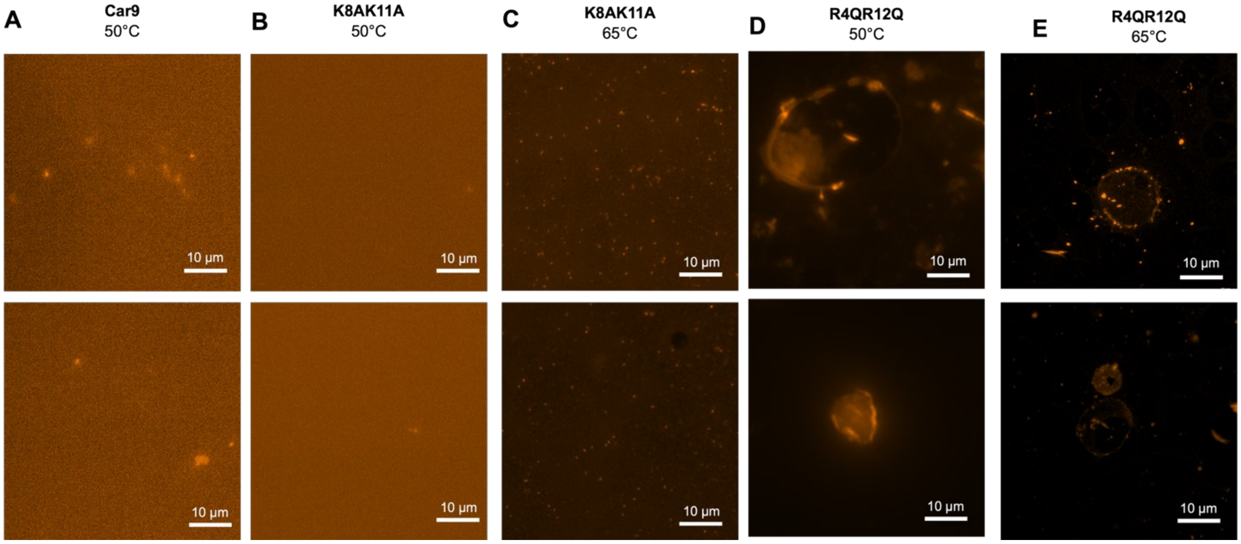

Figure S7. Additional confocal fluorescence microscopy images of Nile red-stained samples prepared with the indicated proteins and at the specified temperatures.

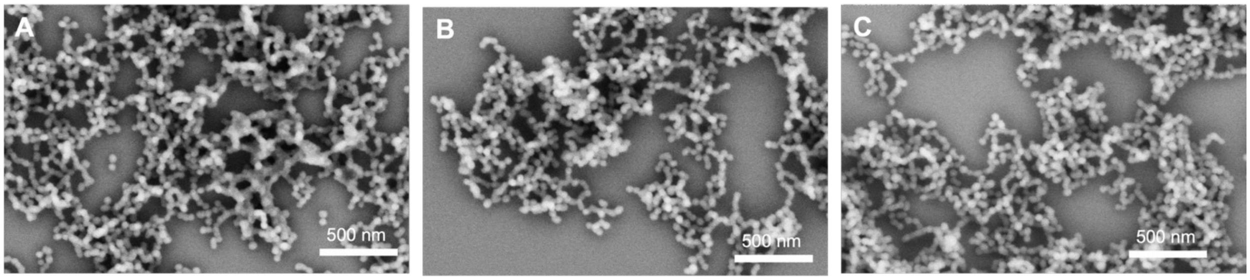

Figure S8. SEM images of V54-K8AK11A mineralization products at 65°C after (A) 30 min, (B) 8 hr, and (C) 24 hr of mineralization.

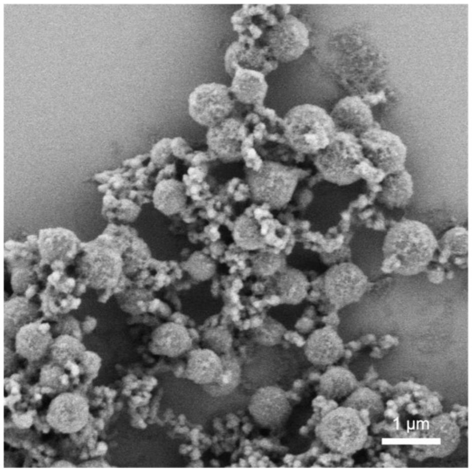

Figure S9. SEM image of V54-K8AK11A mineralization products at 75°C.

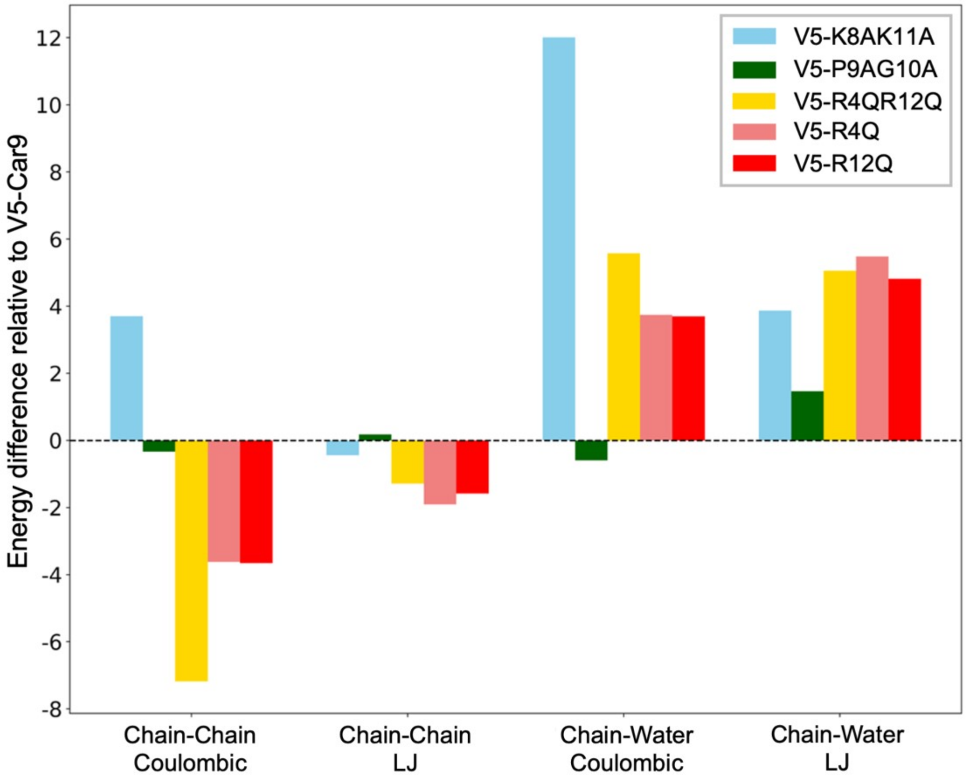

Figure S10. Changes in short-range Coulombic and Lennard Jones (LJ) energies for the indicated surrogates relative to the wild type. Calculations were performed using equation **S1**.

Figure S11. Additional AlphaFold 3.0 predictions for V10-Car9 variants (A) P9AG10A, (B) K8AK11A, (C) R12Q, and (D) R4Q.

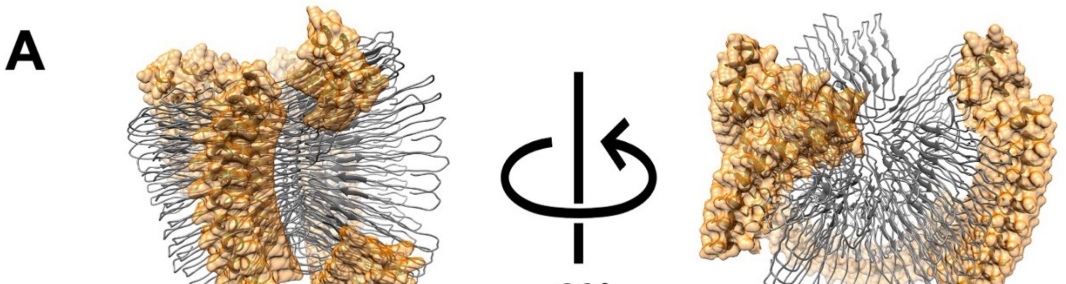

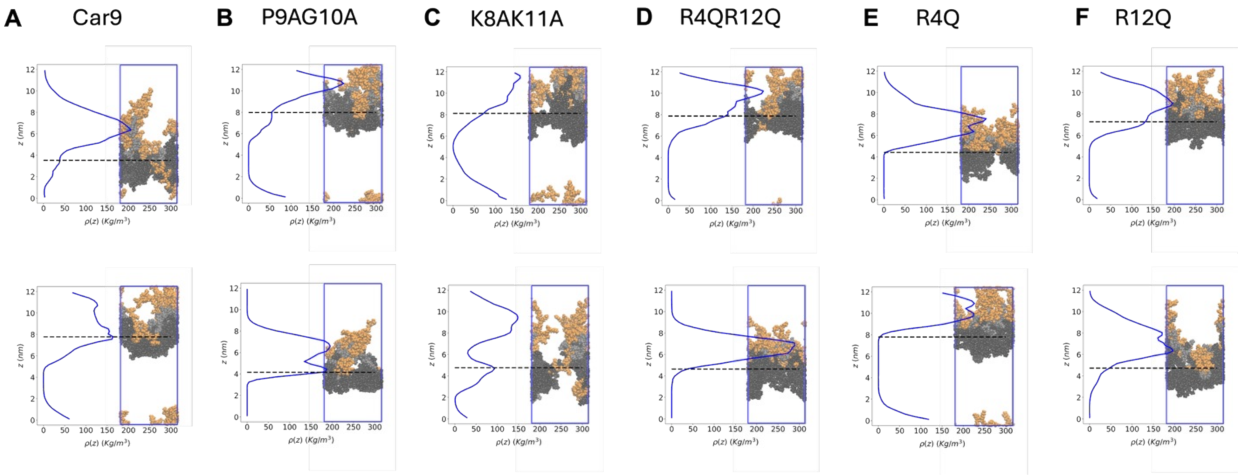

Figure S12. Final density profiles and equilibrium structures for two additional runs of MD simulations with the indicated surrogates.

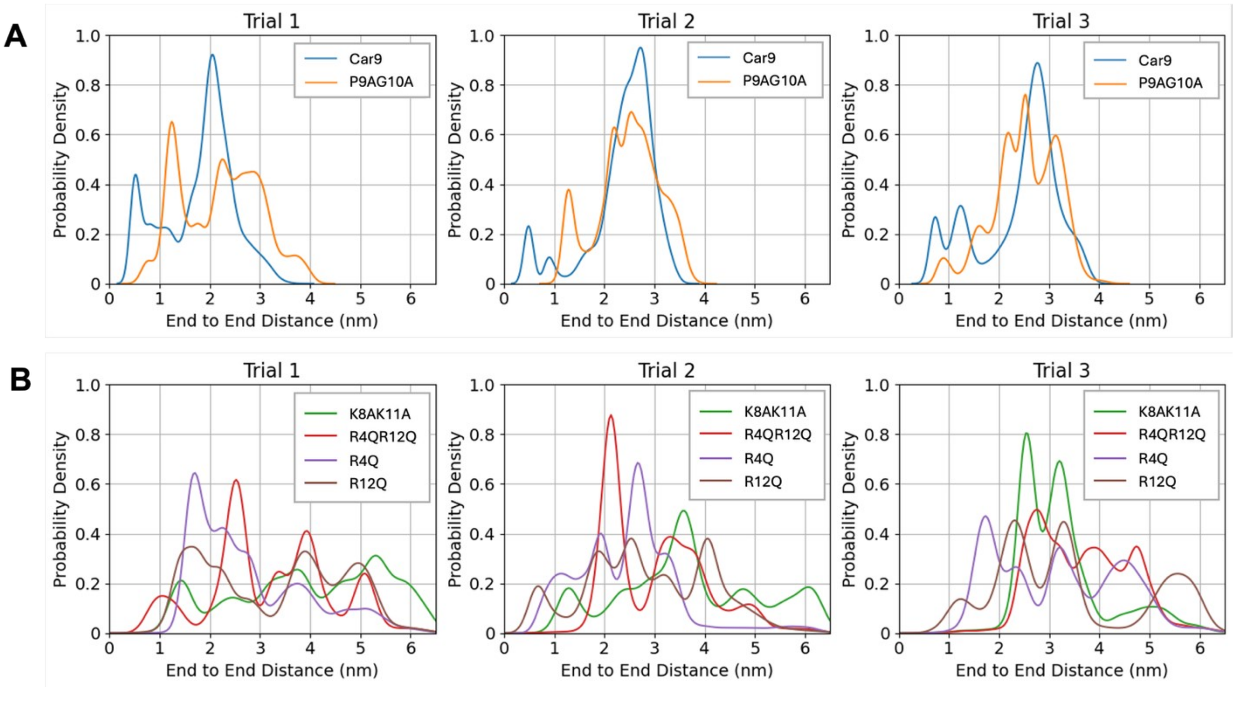

Figure S13. End-to-end distance distributions over the final 100 ns of simulation time across each of three trials for (A) Car9, P9AG10A, (B) K8AK11A, R4QR12Q, R4Q, and R12Q. Variants with smaller characteristic end-to-end distances are more compact, which is related to a greater tendency towards self-association.

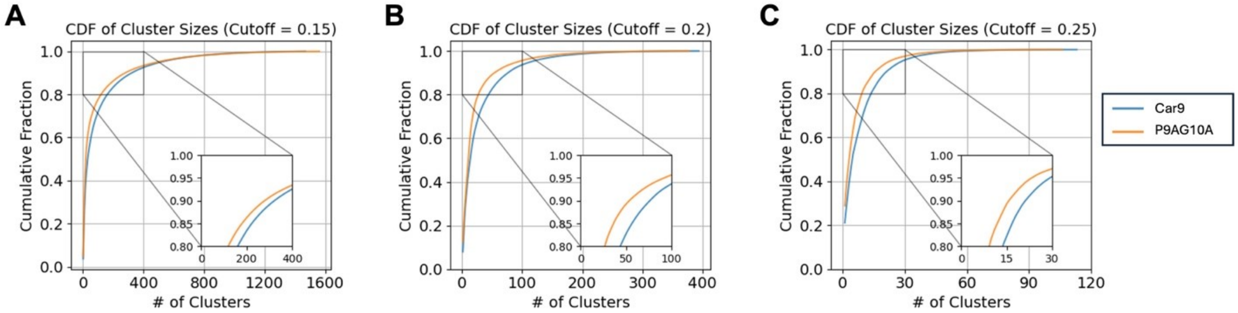

Figure S14. Cumulative distribution functions of cluster sizes, pooling the final 100 ns of triplicate simulation runs for all nine chains in the box (2.7 μs total simulation time), with distance cutoffs of (A) 0.15, (B) 0.20, and (C) 0.25 nm. A steeper slope in the distribution indicates the chain adopts a less diverse set of conformations.

Table S2. Shannon entropy of each variant across 2.7 μs trajectories, at various distance cutoffs.

Peptide	$H_{cutoff = 0.15\,nm}$
Car9	7.767
P9AG10A	7.288
K8AK11A	6.897
R4Q	7.096
R12Q	6.949
R4QR12Q	7.300

References

(1) Hess, B.; Bekker, H.; Berendsen, H. J. C.; Fraaije, J. G. E. M. LINCS: A Linear Constraint Solver for Molecular Simulations. *J. Comput. Chem.* **1997**, *18* (12), 1463–1472. https://doi.org/10.1002/(SICI)1096-987X(199709)18:12%253C1463::AID-JCC4%253E3.0.CO;2-H.

(2) Darden, T.; York, D.; Pedersen, L. Particle Mesh Ewald: An N·log(N) Method for Ewald Sums in Large Systems. *J. Chem. Phys.* **1993**, *98* (12), 10089–10092. https://doi.org/10.1063/1.464397.

(3) Bussi, G.; Donadio, D.; Parrinello, M. Canonical Sampling through Velocity Rescaling. *J. Chem. Phys.* **2007**, *126* (1), 014101. https://doi.org/10.1063/1.2408420.

(4) Berendsen, H. J. C.; Postma, J. P. M.; Van Gunsteren, W. F.; DiNola, A.; Haak, J. R. Molecular Dynamics with Coupling to an External Bath. *J. Chem. Phys.* **1984**, *81* (8), 3684–3690. https://doi.org/10.1063/1.448118.

(5) Chatterjee, S.; Debenedetti, P. G.; Stillinger, F. H.; Lynden-Bell, R. M. A Computational Investigation of Thermodynamics, Structure, Dynamics and Solvation Behavior in Modified Water Models. *J. Chem. Phys.* **2008**, *128* (12), 124511. https://doi.org/10.1063/1.2841127.

(6) Daura, X.; Gademann, K.; Jaun, B.; Seebach, D.; van Gunsteren, W. F.; Mark, A. E. Peptide Folding: When Simulation Meets Experiment. *Angew. Chem. Int. Ed.* **1999**, *38* (1–2), 236–240. https://doi.org/10.1002/(SICI)1521-3773(19990115)38:1/2%253C236::AID-ANIE236%253E3.0.CO;2-M.

(7) Baruah, A.; Rani, P.; Biswas, P. Conformational Entropy of Intrinsically Disordered Proteins from Amino Acid Triads. *Sci. Rep.* **2015**, *5* (1), 11740. https://doi.org/10.1038/srep11740.

(8) Naser, N. Y.; Wixson, W. C.; Larson, H.; Cossairt, B. M.; Pozzo, L. D.; Baneyx, F. Biomimetic Mineralization of Positively Charged Silica Nanoparticles Templated by Thermoresponsive Protein Micelles: Applications to Electrostatic Assembly of Hierarchical and Composite Superstructures. *Soft Matter* **2025**, *21* (2), 166–178. https://doi.org/10.1039/D4SM00907J.